remote sensing

MDPI

Article

Global Intercomparison of Hyper-Resolution ECOSTRESS Coastal Sea Surface Temperature Measurements from the Space Station with VIIRS-N20

Nicolas Weidberg [1,2,*], David S. Wethey [1] and Sarah A. Woodin [1]

[1] Department of Biological Sciences, University of South Carolina, Columbia, SC 29208, USA; wethey@biol.sc.edu (D.S.W.); woodin@biol.sc.edu (S.A.W.)
[2] Coastal Ecology Group, Faculty of Marine Sciences, University of Vigo, 36310 Vigo, Spain
* Correspondence: weidberg@uvigo.es

Abstract: The ECOSTRESS multi-channel thermal radiometer on the Space Station has an unprecedented spatial resolution of 70 m and a return time of hours to 5 days. It resolves details of oceanographic features not detectable in imagery from MODIS or VIIRS, and has open-ocean coverage, unlike Landsat. We calibrated two years of ECOSTRESS sea surface temperature observations with L2 data from VIIRS-N20 (2019–2020) worldwide but especially focused on important upwelling systems currently undergoing climate change forcing. Unlike operational SST products from VIIRS-N20, the ECOSTRESS surface temperature algorithm does not use a regression approach to determine temperature, but solves a set of simultaneous equations based on first principles for both surface temperature and emissivity. We compared ECOSTRESS ocean temperatures to well-calibrated clear sky satellite measurements from VIIRS-N20. Data comparisons were constrained to those within 90 min of one another using co-located clear sky VIIRS and ECOSTRESS pixels. ECOSTRESS ocean temperatures have a consistent 1.01 °C negative bias relative to VIIRS-N20, although deviation in brightness temperatures within the 10.49 and 12.01 µm bands were much smaller. As an alternative, we compared the performance of NOAA, NASA, and U.S. Navy operational split-window SST regression algorithms taking into consideration the statistical limitations imposed by intrinsic SST spatial autocorrelation and applying corrections on brightness temperatures. We conclude that standard bias-correction methods using already validated and well-known algorithms can be applied to ECOSTRESS SST data, yielding highly accurate products of ultra-high spatial resolution for studies of biological and physical oceanography in a time when these are needed to properly evaluate regional and even local impacts of climate change.

Keywords: SST; upwelling; ECOSTRESS; VIIRS; spatial autocorrelation; regression algorithm

Citation: Weidberg, N.; Wethey, D.S.; Woodin, S.A. Global Intercomparison of Hyper-Resolution ECOSTRESS Coastal Sea Surface Temperature Measurements from the Space Station with VIIRS-N20. *Remote Sens.* **2021**, *13*, 5021. https://doi.org/10.3390/rs13245021

Academic Editor: Hirokazu Yamamoto

Received: 29 September 2021
Accepted: 5 December 2021
Published: 10 December 2021

1. Introduction

The pace at which the global ocean is warming due to the anthropogenic greenhouse effect is 0.13 °C per decade [1–3]. Sea surface temperature (SST) rise due to atmospheric warming has been pervasive across all oceans [4] even though it is estimated that a third of global CO_2 emissions from 1994 to 2007 has been sequestered by them [5]. Such warming has resulted in an increase in sea level height and global wave energy [6–8].

In this context, satellites have been a fundamental tool to obtain SST measurements worldwide, thus, allowing the estimation of SST temporal trends at regional to global scales. The first generation of thermal infrared instruments on satellites were developed as early as the 1970s, followed by infrared radiometers with a better resolution and sensitivity on polar orbiting spacecrafts [9,10]. Among these, the Advanced Very High Resolution Radiometer (AVHRR) increased the resolution to 1 km [11]. On the NOAA satellites, AVHRR instruments have been replaced by the Visible Infrared Imaging Radiometer Suite

(VIIRS) since 2011. VIIRS instruments introduced several technical improvements that allowed the study of submesoscale SST features for the first time [12].

However, the ability of satellite products to resolve fine scale structures close to coasts has been limited. Especially in coastal upwelling regions, thermal inversions due to cold coastal waters have caused positive biases in SST measurements from NOAA satellites since the early 1980s [13,14]. As this error is not constant across different temperature ranges, it can severely affect our estimations of long-term trends in SST at these regions. To account for these errors, new products have been developed to characterize coastal SST temporal variability in coastal regions worldwide, such as the Reynolds 0.25 v.2 from NOAA [15], although still with a coarse spatial resolution of 0.25°. Proper quantification of SST trends in upwelling systems is crucial for understanding how the upwelling process interacts with global warming, which has been strongly debated and may severely affect a wide range of fisheries in these productive systems [16–18]. First, it was hypothesized that the intensification of sea-land thermal breezes due to land warming would lead to stronger upwelling events, and therefore cooling of the coastal ocean [19]. Nevertheless, it has been shown that enhanced thermal stratification can effectively compensate upwelling intensification [20,21]. Most likely, these opposing dynamics may drive warming or cooling in different regions within each upwelling system, thus, increasing fine scale spatial heterogeneities [22,23].

Thus, researchers need satellite products with great coverage and increased spatial resolution that can reveal contrasting SST long-term trends at upwelling systems and other oceanic and coastal areas. The ECOsystem Spaceborne Thermal Radiometer Experiment on Space Station (ECOSTRESS) with the Prototype HyspIRI Thermal Infrared Radiometer (PHyTIR) with a pixel size of 70 × 70 m can be potentially used for long-term SST monitoring of different regions of interest. The orbit of the International Space Station provides good coverage from the tropics to 52° approximately with a mean revisit interval of 4–5 days, depending on latitude. Three spectral bands have been available since May 2019: 8.78, 10.49, and 12.09 µm. The temperature emissivity separation (TES) algorithm used to derive surface temperatures on land and sea from brightness temperature measurements and other parameters is described in detail in [24]. It has been validated mainly on land surfaces [25] and in relatively small inland water bodies such as Lake Tahoe [26], and at sea off the coasts of Florida [27], but not on a global scale.

A multisensor intercomparison is one of the methodologies recommended by the Committee of Earth Observation Satellites Working Group on Calibration and Validation to validate surface temperature datasets [25]. Although this method does not provide absolute calibrations, it is useful to infer instrument biases and to compare different algorithm outputs. In this study, we validate and calibrate a large and representative ECOSTRESS SST dataset with a satellite product widely used in oceanographic studies, the VIIRS-N20 with 750 m spatial resolution. This product was chosen for this global comparison because of its small and stable bias and because it has been providing good quality SST data since it was launched in November 2017 [28]. It has seven bands from 3.6 to 12.5 µm [29] and VIIRS instruments have shown a small uncertainty in SST measurements of 0.1 K [30,31]. In addition, the black body in these instruments goes through a periodic warm-up/cool-down procedure to check calibration coefficients [31]. Currently, VIIRS imagery is being used to build a multisensor product for the Australian Bureau of Meteorology [32] and constitutes an important source for the Operational Sea Surface Temperature and Sea Ice Analysis (OSTIA [33]). Thus, using VIIRS-N20 as a reference product, our main aims were (1) to identify ECOSTRESS SST biases across a wide range of temperatures in the main upwelling systems of the world and other regions of interest, (2) to infer the nature of these biases, and (3) to propose the use of other algorithms commonly used in other satellite SST products and select the best combination of parameters to derive SST from ECOSTRESS input data.

2. Materials and Methods

2.1. Data Acquisition and Processing

A total of 35 ECOSTRESS swath (L2) images from February 2019 to July 2020 in seven different coastal regions were selected to be compared with quasi-simultaneous VIIRS-N20 swath (L2) images taken within 90 min before/after the corresponding ECOSTRESS image (Table S1). These seven regions were California, Chile, Bay of Biscay/English Channel, Eastern Mediterranean, South Africa, Gulf of Arabia, and Okhotsk Sea (Figure 1). They were selected based on the availability of ECOSTRESS imagery and in order to span the worldwide range of SST from 0 to 35 °C. Four different files were retrieved from the ECOSTRESS archive (https://ecostress.jpl.nasa.gov/data/, accessed on 7 December 2021) for each image: CLD (cloud mask) [34], LSTE (land-sea temperature) [35], RAD (radiance) [36], and GEO (geolocation) [37]. The VIIRS files [38,39] were retrieved from the NASA Physical Oceanography Distributed Active Archive Center (PODAAC).

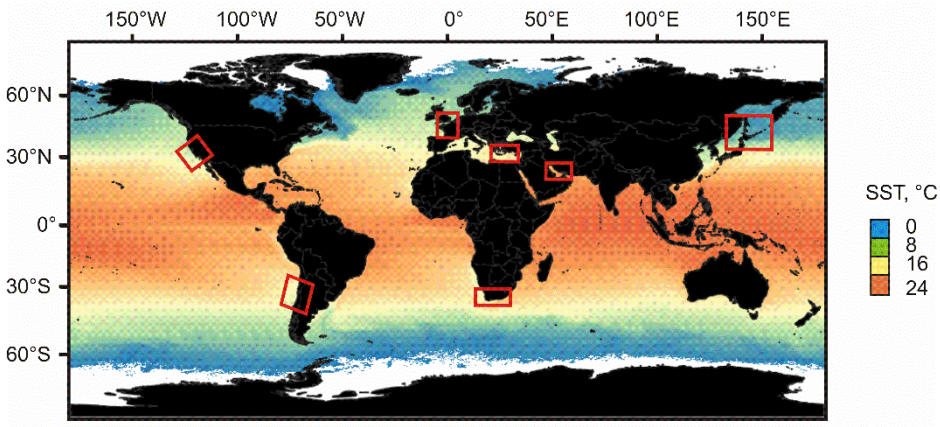

Figure 1. Worldwide map showing the mean sea surface temperatures from 20 March 2012 to 20 June 2019 retrieved from the VIIRS sensor on the SNNP satellite with a spatial resolution of 4 km. The red squares show the 7 regions where ECOSTRESS-VIIRS comparisons were performed.

The ECOSTRESS cloud mask and the VIIRS quality layer were used to eliminate pixels with erroneous data from the comparisons. Thus, only ECOSTRESS cloud-free pixels and VIIRS-N20 L5 pixels were used in these analyses. To check the reliability of the VIIRS-N20 data used for the comparisons, daily values of VIIRS-N20 SST bias with respect to the drifter and tropical moorings dataset from NOAA were inspected for the whole study period (https://www.star.nesdis.noaa.gov/socd/sst/squam/polar/viirs/, accessed on 7 December 2021). As detailed below, no outliers greater than 0.15 or less than −0.05 °C were found.

SSTs, brightness temperatures at 10.49 and 12.09 μm (hereafter BT11 and BT12), and zenith angle (hereafter ZA) for ECOSTRESS pixels were obtained for a total of 2,282,366 individual ECOSTRESS-VIIRS pixel matchups from the 35 images. In addition, for each of these comparisons, daily SST L4 analysis data from the GHRSST group and the Canadian Meteorological Center (CMC) with a spatial resolution of 0.1° [40] were retrieved from PODAAC. This dataset is commonly used as a "first guess" temperature to be incorporated into SST regression algorithms [41].

The VIIRS files were reprojected to UTM using SeaDAS v7.5.3 (https://seadas.gsfc.nasa.gov/, accessed on 7 December 2021), and the ECOSTRESS files were reprojected to UTM using ECOSTRESS_swath2grid.py [42]. Then, nearest neighbor matching of VIIRS pixels to the ECOSTRESS grid was applied by using the spatstat v1.64 package in R [43].

2.2. Spatial Autocorrelation and Brightness Temperature Corrections

Four different datasets were used to characterize ECOSTRESS SST bias with respect to VIIRS-N20 (Table 1). First, the whole dataset with 2,282,368 pixels was used. Second, the mean bias in brightness temperatures (BT) with respect to VIIRS-N20 was corrected by

calculating the mean differences between VIIRS-N20 and ECOSTRESS BT11 and BT12 and adding those differentials to the raw ECOSTRESS BT yielding a brightness temperature corrected dataset. VIIRS brightness temperature measurements were considered to be a reference for this correction because of their stability and reduced bias [31]. Third, autocorrelation functions (ACFs) were applied to discard all spatially autocorrelated data, as temperatures from neighboring pixels were not truly independent, due to continuity of the water environment. Because data from neighboring pixels are not independent, new observations do not add full degrees of freedom [44] and this has to be considered in the data analysis. Thus, e-folding distances were calculated on the X and Y axes for each of the 35 VIIRS-N20 images with the following procedure: Pearson´s R autocorrelation functions were calculated along both axes of the reprojected images with the acf function in the R package stats 3.6.2 [45]. Then, for each pixel row/column in the image, the distances at which inter-pixel SST Pearson´s R correlation coefficients decreased by a factor of e were considered to be the e-folding distances at which SST measurements become decorrelated. Finally, these distances were averaged across all pixel rows/columns to obtain image-specific mean e-folding distances for both axes. Similar procedures have been used to account for temporal autocorrelation in SST anomalies [46,47]. Spatial grids with these distances were specifically built for each image to select independent SST measurements, thus, reducing the dataset from 2,282,368 to 406 observations after correction for autocorrelation. Finally, both the BT and spatial autocorrelation corrections were applied to produce the fourth dataset. In addition, we also split the whole dataset into day and night comparisons to examine potential differences in mean bias as a function of daylight.

2.3. Algorithm Selection

To assess the adequacy of the ECOSTRESS input data to obtain reliable SSTs, ECOSTRESS brightness temperatures, zenith angles, and CMC "first guess" temperatures were used as input predictors of VIIRS-N20 SST data using 5 different algorithms: NAVO, NRL, NLSST, MC, and VIIRS [39].

$$SST = a0 + a1\ BT11 + a2\ \Delta TFG + a3\ \Delta T + a4\ \Delta T\ S\Theta \quad \text{(NAVO)} \quad (1)$$

$$SST = a0 + a1\ BT11 + a2\ \Delta T + a3\ \Delta T\ S\Theta + a4FG \quad \text{(NRL)} \quad (2)$$

$$SST = a0 + a1\ BT11 + a2\ \Delta T + a3\ \Delta TFG + a4\ BT11\ S\Theta + a5\ \Delta T\ S\Theta + a6\ ZA \quad \text{(NLSST)} \quad (3)$$

$$SST = a0 + a1\ BT11 + a2\ \Delta T + a3\ \Delta T\ S\Theta \quad \text{(MC)} \quad (4)$$

$$SST = a0 + a1\ BT11 + a2\ \Delta TFG + a3\ S\Theta + a4\ ZA + a5\ ZA2 \quad \text{(VIIRS)} \quad (5)$$

In this way, we calculated new ECOSTRESS SST estimates using VIIRS-N20 SST data as references with published regression algorithms and not with the ECOSTRESS TES algorithm. Depending on the algorithms, more complex parameters were required and derived from ECOSTRESS input variables: ΔT (BT11–BT12), SΘ (sec (ZA)–1), ZA2 (the square of the zenith angle), ΔTFG (ΔT × FG), and ΔT SΘ (ΔT × SΘ). The statistical significance of all these parameters was evaluated through analysis of variance with a type III sum of squares so that coefficient estimates were all calculated last (after accounting for all other variables). These coefficient estimates were also compared with those obtained from other published studies performed with VIIRS instruments [48] and from those obtained at the Community Satellite Processing Package (https://cimss.ssec.wisc.edu/cspp/acspo_v1.2.shtml, accessed on 7 December 2021) and the Long Wave SST algorithm webpage (https://oceancolor.gsfc.nasa.gov/atbd/sst/#sec_2, accessed on 7 December 2021). In addition, the Bayesian information criteria (BIC) was calculated to rank the performance of each algorithm by favoring increments in the goodness of fit (R^2) and penalizing model complexity (the number of parameters in the model). In addition, BIC accounts for the number of observations (N) in the analysis, as the degrees of freedom are k = ln (N), instead of k = ln (2)), as in the Akaike information criterion (AIC, MASS package [45]). In addition, a backward removal parameter procedure based on BIC and starting with a model containing all the parameters was applied for each of the 4 datasets.

A maximum of 100 steps were given to the step function in R (MASS package [45]) to determine to the model with the best performance.

Table 1. Main parameters for 4 different SST algorithms obtained from published studies on VIIRS instruments, and from our analyses with ECOSTRESS input data taking into consideration the whole dataset (ALL DATASET), a reduced dataset after a correction based on the e-folding autocorrelation distance (CORRECTED ACF), a full dataset with a correction of the mean bias of brightness temperatures (CORRECTED BT) and with a reduced dataset after applying both corrections (CORRECTED ACF BT). Numbers in bold show coefficient values for significant parameters.

Algorithm	Variables	Published Coefficient Values (Ranges When Available)	All Dataset	Corrected ACF	Corrected BT	Corrected ACF BT
NAVO	Intercept	−269.4435 to −268.1847	**2.9864**	**3.1315**	**2.972**	**3.3266**
	BT11	0.9863 to 0.9910	**0.9909**	**0.9710**	**0.9732**	**0.9575**
	ΔT	0.3772 to 0.4586	**−0.4285**	**−0.6557**	**−0.4623**	**−0.5379**
	ΔTFG	0.722 to 0.765	**0.0296**	**0.0461**	**0.03051**	**0.0404**
	ΔTSΘ	−0.2485 to −0.2201	**−0.2256**	**1.1759**	**0.186**	**0.9034**
NRL	Intercept	−205 to −5	**21.9000**	**2.4551**	**1.8797**	**2.4337**
	BT11	0.021 to 0.752	**0.9300**	**1.0186**	**0.9348**	**1.0186**
	ΔT	0.018 to 1.9	**0.1700**	**0.1973**	**0.1627**	**0.2080**
	ΔTSΘ	0.005 to 0.853	**−0.1800**	1.0539	**0.1811**	**0.9045**
	FG	0.259 to 0.911	**0.0800**	0.0009	**0.0891**	0.0006
MC	Intercept	1.75	**2.4980**	**2.4578**	**2.1660**	**2.4355**
	BT11	1.009	**1.0290**	**1.0195**	**1.0210**	**1.0193**
	ΔT	2.475	**0.1780**	**0.1974**	**0.1585**	**0.2081**
	ΔTSΘ	1.282	**−0.3100**	1.0536	**0.1206**	**0.9044**
NLSST	Intercept	0.985192	**2.8289**	**3.1843**	**2.6930**	**3.3984**
	BT11	0.019775	**0.9741**	**0.9622**	**0.9546**	**0.9475**
	BT11SΘ	0.456758	**0.3054**	0.1569	**0.3344**	0.1564
	ΔT	0.067732	**−0.1726**	**−0.5877**	**−0.2173**	**−0.5039**
	ΔTFG	0.705117	**0.0306**	**0.0466**	**0.0314**	**0.0416**
	ΔTSΘ	−4.714369	**−5.1816**	−0.3961	**−4.6510**	−0.2481
	ZA	5.623045	**0.5628**	−0.1656	**0.9899**	−0.1626
VIIRS	Intercept	63.6091 to 7.7597	**−87.0400**	6.4098	**−87.5900**	5.7413
	BT11	21.7769 to 3.2434	**1.0080**	**0.9953**	**1.0000**	**0.9870**
	ΔTFG	0.5460 to 0.4679	**0.0112**	**0.0191**	**0.0117**	**0.0187**
	SΘ	0.7086 to 0.4124	**89.5400**	−3.6364	**89.8300**	−2.9009
	ZA	0.6568 to 0.3256	**1.9620**	−1.7518	**1.9770**	−1.7160
	ZA2	0.0003 to -5.17×10^{-5}	**−51.8700**	6.1414	**−52.0500**	5.6632

3. Results

3.1. Bias Estimates

The VIIRS-N20 daily SST bias with respect to the drifter and tropical moorings dataset from NOAA ranged from −0.05 to 0.15 °C with a mean of 0.015 °C (Figure 2). Overall, ECOSTRESS had a −1.01 °C SST bias with respect to VIIRS-N20 for the whole dataset. For the reduced dataset after the ACF correction, there was a −1.02 °C SST bias. This deviation can be observed at individual ECOSTRESS-VIIRS comparisons (Figure 3), but it is especially evident when SSTs from both VIIRS-N20 and ECOSTRESS are correlated

(Figure 4). The fit is excellent for the whole dataset (R^2 = 0.99 and RSE = 0.66) and also for the reduced dataset after the ACF correction (R^2 = 0.99 and RSE = 0.51). However, the regression line is always below the 1:1 line (Figure 4A) and, when the bias is plotted as a function of VIIRS SST, it is uniformly distributed along the whole temperature range (Figure 4B). Note, however, that very low unrealistic ECOSTRESS SST values are present, probably due to cloud contamination. Similarly, a relatively uniform bias across brightness temperatures was detected for both BT12 and BT11, although for the former a slight trend towards a larger cold bias at warmer brightness temperatures was apparent (Figure 5). These biases were smaller than those observed for SST: −0.33 for BT12 and 0.23 for BT11 (−0.58 and −0.09, respectively, when the ACF correction was applied). The mean SST bias and bias distribution across the whole temperature range did not change between day (−1.006 °C) and night (−1.03 °C) scenes (Figure 6).

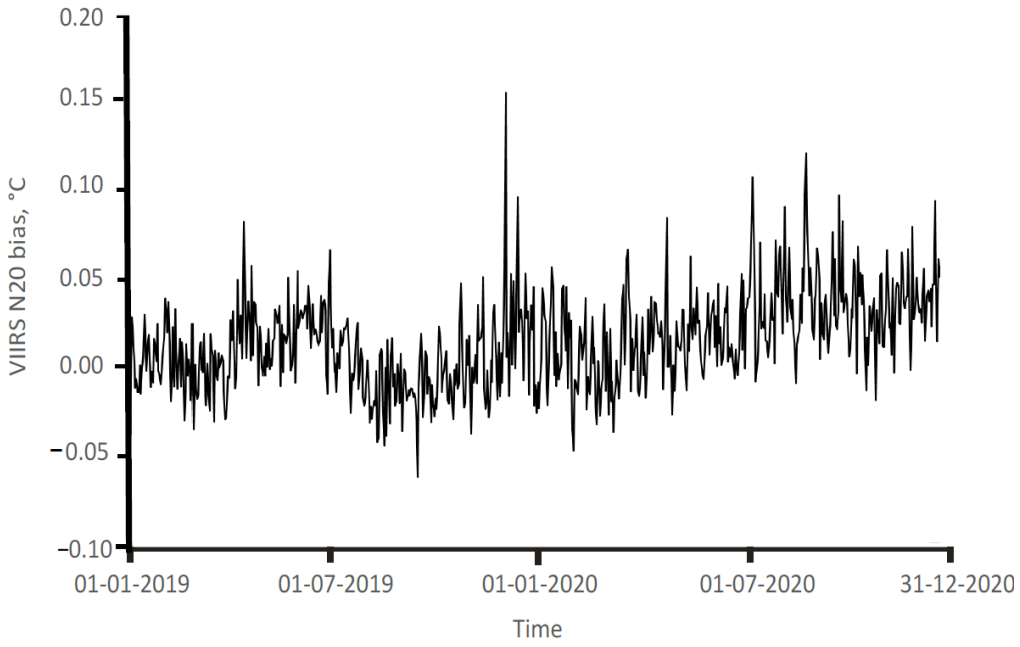

Figure 2. Daily VIIRS-N20 SST bias for the period 2019–2020 with respect to the drifters and tropical mooring NOAA dataset.

3.2. Spatial Autocorrelation Distances and Algorithm Selection

A wide range of e-folding distances was obtained along the horizontal and vertical axes within the sections of the VIIRS images that overlapped with ECOSTRESS images. Specifically, they span from 8 to 114 km in the horizontal axis, and from 27 to 125 km in the vertical axis (Table S1). A total of 406 independent data points were extracted using grids built with these e-folding distances (Figure 7). The coefficients obtained for each of the algorithm parameters using these spatially autocorrelation corrected data points barely overlapped with published values (Table 1), but this was also true for the coefficients obtained with the full dataset as well as the dataset corrected for brightness temperature bias. In some cases, such as the parameter BT11 for NAVO, only the estimated coefficient for the full dataset was within the range of published coefficient values. On the one hand, in 12 out of the 16 estimations with ranges, none of the estimations for any of the four datasets were within the published range, for example, ΔT for NAVO. On the other hand, only 18 out of the 108 coefficient estimates were non-significant, all of them in the reduced ACF corrected dataset or in the reduced ACF and BT corrected dataset. The reason that the coefficients do not always match the published values is that the spectral responses of the ECOSTRESS channels are not identical to the spectral responses of the instruments for which they were developed. When algorithms were applied to the whole VIIRS-N20 dataset, the NLSST algorithm was selected as the best fit according to BIC scores,

irrespective of the biases in BT11 and BT12 being corrected or not. However, when the reduced ACF corrected dataset was analyzed, then, the NAVO algorithm was selected as the best fit (Table 2 and Figure 8). Nevertheless, R^2 always exceeded 99% of the total variability explained, regardless of the specific algorithm that was applied (Table 2 and Figure 8). The results of the algorithm selection process by backward BIC show that the model containing all nine of the parameters from all the algorithms was selected as the best for the whole dataset, a more complicated model than any of these (Model 1, Table 3). However, an equally good model with only 5 parameters was obtained for the reduced ACF corrected dataset regardless of the BT correction: FG, BT11, ΔT, ΔTFG, and BT11SΘ (Model 2, Table 3). Neither of these last two models corresponds to the regression models typically used [39].

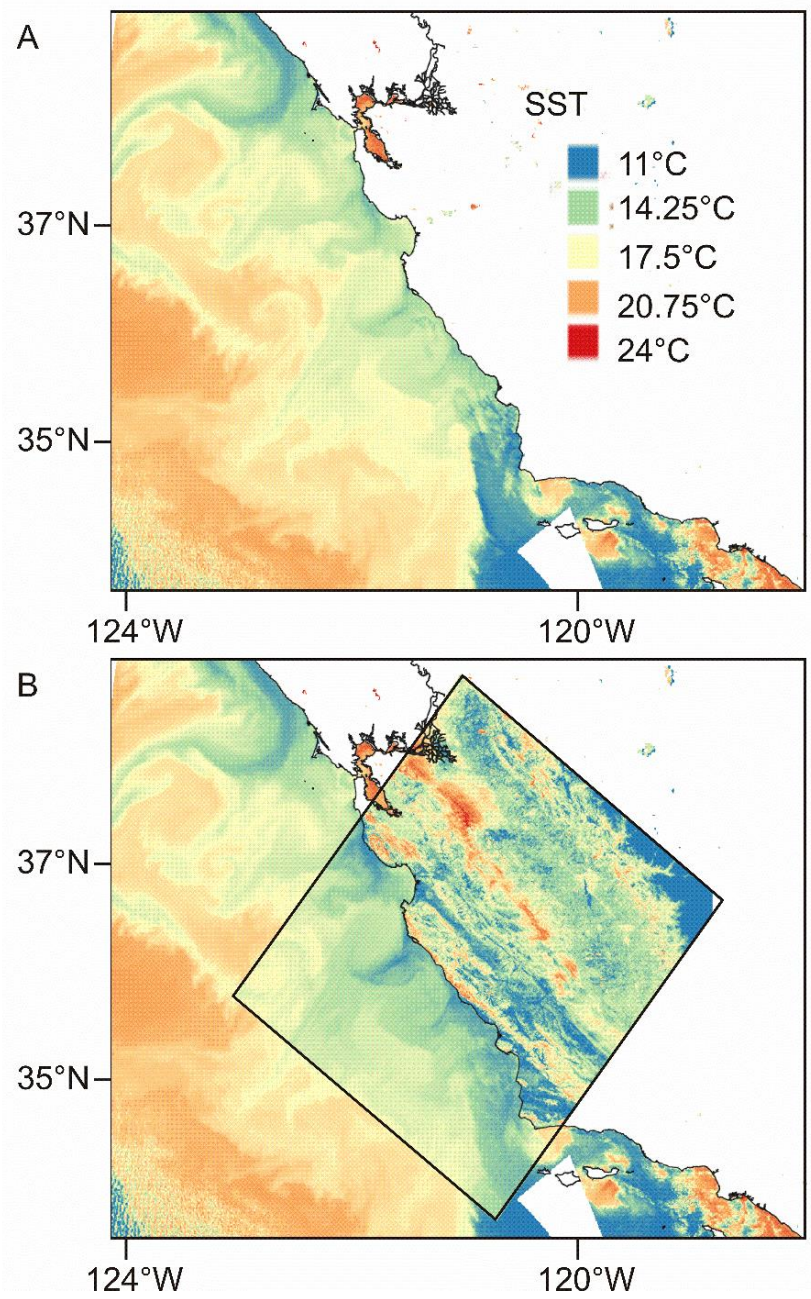

Figure 3. Example of the comparison of ECOSTRESS to VIIRS-N20: (**A**) VIIRS-N20 image off the coast of California on 24 September 2019 09:10 UTC; (**B**) same image with a superimposed quasi-simultaneous ECOSTRESS image taken at 08:49 UTC.

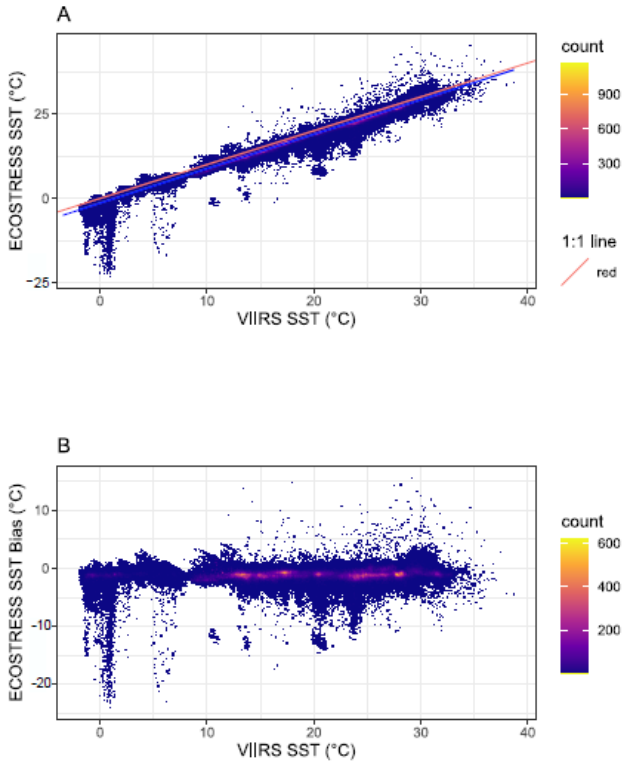

Figure 4. (**A**) ECOSTRESS SST data correlated against VIIRS SST data. Blue and red lines represent the regression line and the 1:1 line; (**B**) ECOSTRESS bias with respect to VIIRS SST data. Colors indicate the number of observations.

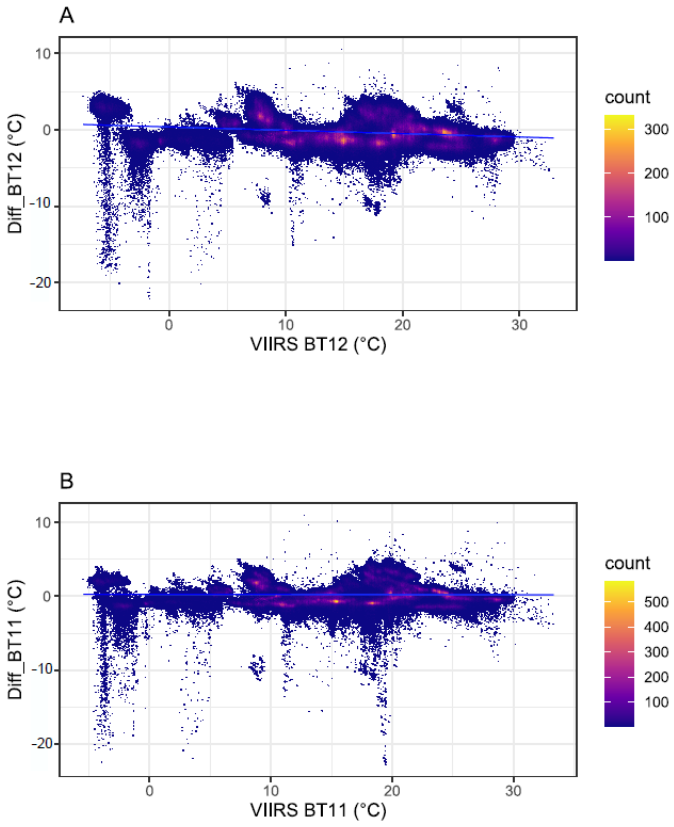

Figure 5. Bias distributions in (**A**) BT12 and (**B**) BT11 as a function of VIIRS brightness temperatures. Blue lines show linear regression fits. Colors indicate the number of observations.

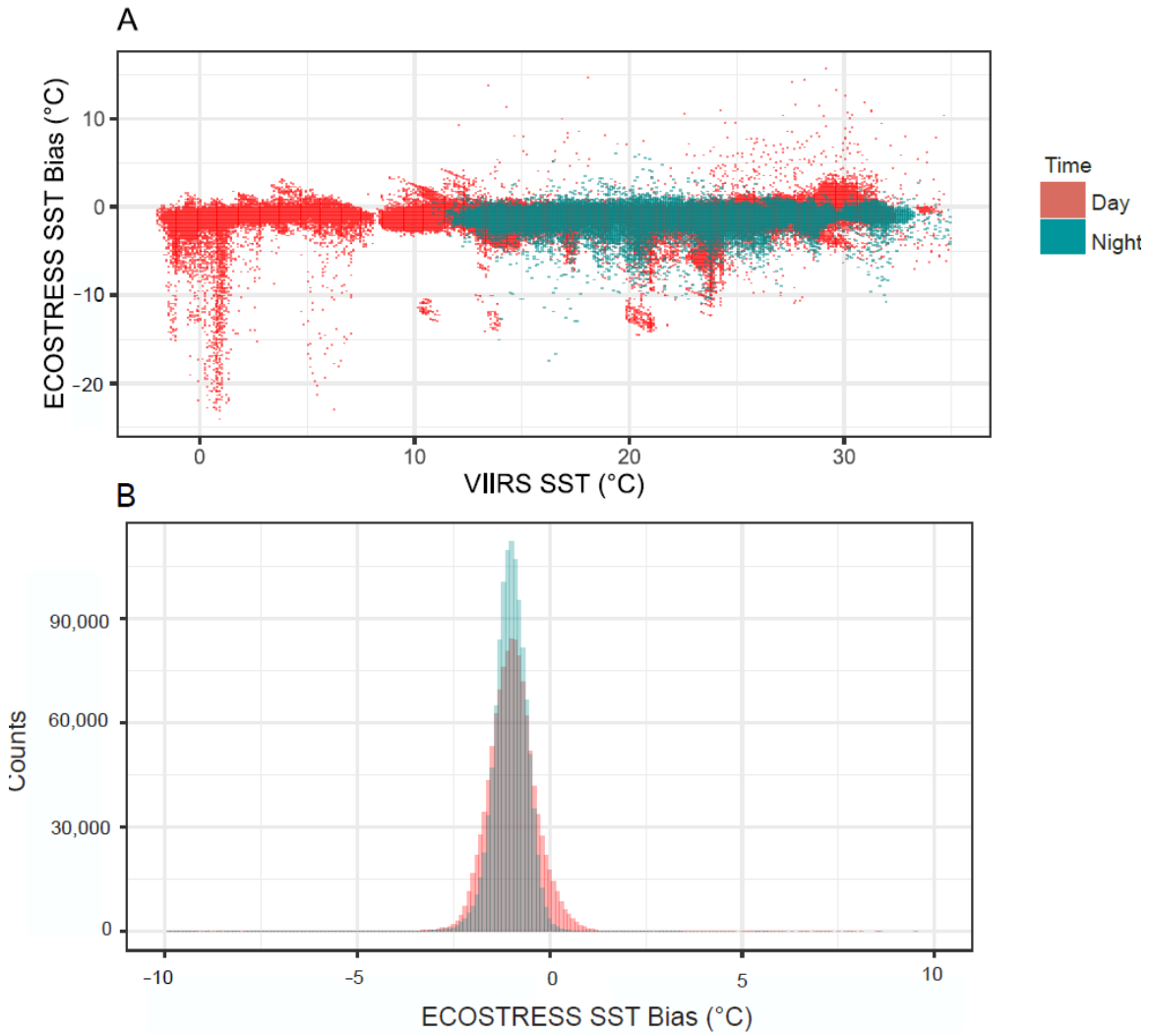

Figure 6. (**A**) ECOSTRESS bias with respect to VIIRS SST data as a function of time (day/night). (**B**) Histograms of ECOSTRESS bias relative to VIIRS SST. Color of overlapping areas is grey.

Table 2. Bayesian information criterion (BIC), R^2, and RSE for all the algorithms used to fit VIIRS-N20 SST with ECOSTRESS input data taking into consideration the whole dataset (ALL DATASET), a reduced dataset after a correction based on the e-folding autocorrelation distance (CORRECTED_ACF), the whole dataset with a correction of the mean bias of brightness temperatures (CORRECTED_BT), and a reduced dataset after applying both corrections (CORRECTED_ACF_BT). Numbers in bold show the best fit for each dataset.

	ALL DATASET			**CORRECTED_ACF**			**CORRECTED_BT**			**CORRECTED_ACF_BT**		
	BIC	**R^2**	**RSE**	**BIC**	**R^2**	**RSE**	**BIC**	**R^2**	**RSE**	**BIC**	**R^2**	**RSE**
NAVO	4,619,031	0.9903	0.6684	**524.679**	**0.996**	**0.4528**	4,601,196	0.9904	0.6658	**531.0998**	**0.9959**	**0.4565**
NRL	4,615,638	0.9904	0.6679	584.327	0.9954	0.4884	4,615,226	0.9904	0.6678	582.7101	0.9954	0.4874
MC	4,694,935	0.99	0.6796	578.353	0.9954	0.4878	4,695,826	0.99	0.6798	576.734	0.9954	0.4868
NLSST	**4,509,200**	**0.9908**	**0.6524**	532.667	0.996	0.4517	**4,503,904**	**0.9908**	**0.6517**	539.7204	0.996	0.4558
VIIRS	4,618,481	0.9902	0.6741	548.429	0.9958	0.4638	4,608,488	0.9904	0.6668	549.8548	0.9958	0.4646

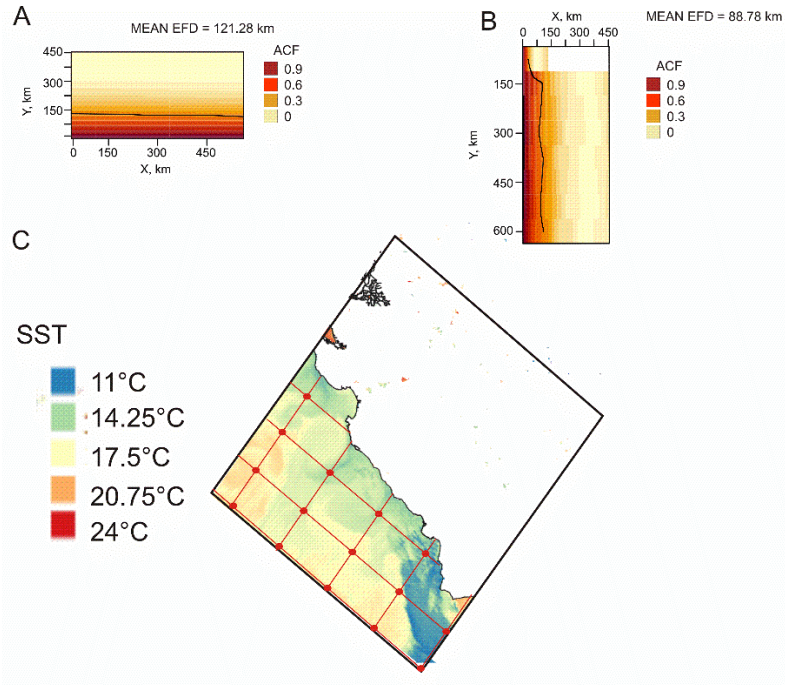

Figure 7. Spatial autocorrelation analyses on VIIRS-N20 image overlapping with a collocated quasi-simultaneous ECOSTRESS image on 24 September 2019: (**A**) ACF contour plots in the Y axis, with a contour line indicating e-folding distance (EFD) and showing mean EFD for this axis; (**B**) same for X axis; (**C**) VIIRS-N20 section overlapping with the quasi-simultaneous ECOSTRESS image.

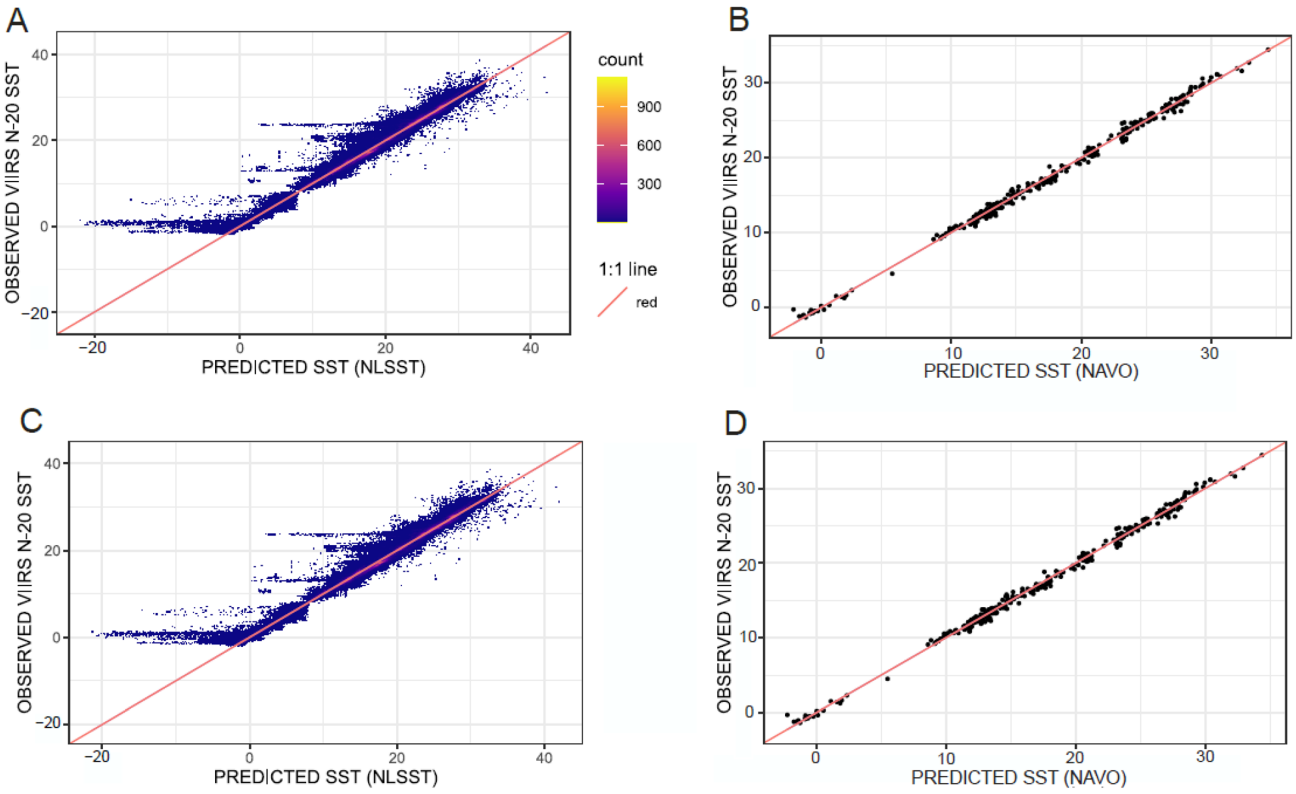

Figure 8. Correlations of observed VIIRS SST against predicted SST data inferred from ECOSTRESS input data using different algorithms. Note, only the best results according to BIC are shown for each dataset: (**A**) NLSST for the whole dataset; (**B**) NAVO for the reduced dataset corrected by autocorrelation functions; (**C**) NLSST for the whole dataset with corrected brightness temperatures; (**D**) NAVO for the reduced dataset corrected by autocorrelation function with corrected brightness temperatures. Red line is the 1:1 line. Colors indicate the number of observations.

Table 3. Best models (Models 1 and 2) from the backward BIC model selection performed on each of the 4 datasets. None of these 2 models is identical to the traditional SST regression algorithms. Significant F values are shown in bold. BIC values are the ones obtained when removing the corresponding parameter from the whole model. Within each model, parameters are ordered following ascending BIC values, that is, from worse to better performance of each parameter within its corresponding model.

ALL DATASET	Df	Sum of Sq	F Value	BIC
Whole model (Model 1)				155,937.8
ΔT	12,273,036	12	**29.989**	155,993.8
ZA	12,273,036	1464	**3512.8**	156,068.8
ZA2	12,273,036	2609	**6259.3**	156,154.8
SΘ	12,273,036	2938	**7049.8**	156,180.8
ΔTFG	12,273,036	17,728	**41454**	156,778.8
BT11SΘ	12,273,036	8910	**21377**	156,802.8
FG	12,273,036	14,496	**7049.8**	157,565.8
ΔTSΘ	12,273,036	34,816	**83532**	159,294.8
BT11	12,273,036	3,483,731	**8,358,400**	273,827.8
ACF CORRECTED				
Whole model (Model 2)				526.3848
FG	1388	1.34	**6.7039**	527.1348
BT11SΘ	1388	1.63	**8.1236**	528.5548
ΔT	1388	6.67	**33.2962**	552.8248
ΔTFG	1388	14.46	**72.1608**	587.5948
BT11	1388	640.85	**3198.5076**	1396.6148
BT CORRECTED				
Whole model (Model 1)				4,461,493
ΔT	12,273,036	12	**29.989**	4,461,517
ZA	12,273,036	1464	**3512.8**	4,464,997
ZA2	12,273,036	2609	**6259.3**	4,467,738
SΘ	12,273,036	3198	**7672.1**	4,469,146
FG	12,273,036	7648	**18,350**	4,479,763
BT11SΘ	12,273,036	8910	**21,377**	4482,764
ΔTFG	12,273,036	17,278	**41,454**	4,502,568
ΔTSΘ	12,273,036	34,816	**83,532**	4,543,521
BT11	12,273,036	3,483,731	**8,358,400**	7,968,110
ACF_BT CORRECTED				
Whole model (Model 2)			**77.74**	526.3848
BT11SΘ	1388	1.63	**8.1218**	528.5548
FG	1388	2.76	**13.7922**	534.1548
ΔT	1388	6.68	**33.3154**	552.8448
ΔTFG	1388	14.46	**72.1838**	587.6148
BT11	1388	640.55	**3197.008**	1396.4548

4. Discussion

4.1. Bias Magnitude and Nature

The comparisons performed between ECOSTRESS and VIIRS-N20 imagery worldwide indicate that ECOSTRESS presents a mean bias of −1.01 °C that is uniform across the whole SST range from 0 to 35 °C (Figures 3 and 4). Regardless of corrections for spatial autocorrelation, the −1 °C bias in SST remained. Additionally, there is a bias in the ECOSTRESS BT11 and the BT12 measurements (Figure 5), as previously discussed by [25,26], though our estimates of the bias differ from theirs as discussed below. Application of standard regression algorithms resulted in unbiased SST estimates from ECOSTRESS input data with VIIRS SST datasets as a reference. Using the regression algorithms NAVO and NLSST yielded particularly successful results; thus, by replacing the ECOSTRESS TES algorithm with one of the standard regression algorithms the systematic −1 °C bias in SST was eliminated (Figure 8).

ECOSTRESS biases in SST and brightness temperatures have been previously detected using smaller datasets. In fact, greater negative biases than those we reported were found at Lake Tahoe and Salton Sea for BT11 and BT12 measured by in situ radiometers (−0.87 and −0.86 °C, respectively, [26]). Nevertheless, SST biases for these water bodies were smaller than those we observed: −1.01 °C as compared with −0.91 and −0.63 °C at Lake Tahoe and Salton Sea, respectively [25]. On the one hand, in contrast with our observations, the SST negative biases increased at lower temperatures at these sites. On the other hand, the surface temperature biases and trends were markedly reduced when calibrations were performed with in situ radiometers on land surfaces [25]. At sea, SST comparisons were performed between ECOSTRESS and a variety of buoys within Florida Bay [27]. There, an overall bias of −0.83 °C was observed, although it ranged from −1.2 °C at night to −0.58 °C during the day. In this study, buoys were measuring temperatures between 0.5 to 2 m below the surface, which corresponded to slightly colder water masses with respect to the skin temperatures measured by ECOSTRESS. However, such thermal differences have been shown to be typically smaller than 0.5 °C [49], and do not account for the whole bias observed. Furthermore, the bias was only 0.11 °C when these same buoy measurements were compared with MODIS SST imagery rather than ECOSTRESS SST, both measuring skin temperatures [27]. Our results are largely in agreement with these ECOSTRESS-buoys comparisons and the slight differences in bias magnitude and day/night bias contrasts between both studies could be due to the limited number of observations (85) and shorter thermal range (15–35 °C) obtained off Florida.

In addition to ECOSTRESS with its −1 °C bias, negative biases in SST satellite retrievals have been observed with some infrared radiometers. The lack of a 3.7 µm band increases the probability of getting significant biases in SST measurements [50,51]. ECOSTRESS lacks a 3.7 µm band, although a proper characterization of the water vapor absorption vertical profiles in wet atmospheres usually corrects this type of bias even when the 3.7 µm band is lacking [50]. For ECOSTRESS, such characterization is given by the TES algorithm, which retrieves emissivity at each band and SST values from radiance measurements through an iterative process that accounts for atmospheric correction [52]. However, the range of emissivity retrieved by TES algorithms, called the minimum maximum difference (MMD) is usually much broader than that characteristic of ocean surfaces, vegetation, and other graybodies, thus, increasing the probability of getting a large bias. The emissivity of seawater, for example, is typically 0.990 at 10.49 µm; the TES algorithm yields calculated values as low as 0.93 with a mean of 0.98. In these cases, we used the split window deterministic algorithms based on linear regressions inferred from SST measurements, which may have resulted in better, unbiased SST estimates even when brightness temperatures were already biased (Table 2 and Figure 8).

An alternative procedure to using these split window deterministic algorithms may be an iterative radiance-based validation method [25] using the RTTOV model, which uses water vapor profiles from numerical weather predictions or reanalyses for full scale retrievals independently of the radiances [53,54]. For ECOSTRESS, this approach was used

to calculate theoretical sensor differentials between RTTOV simulations of BT11 and BT12 values which were in turn compared with those between BT11 and BT12 real measurements from the ECOSTRESS instrument [25]. If these differentials are essentially the same (<0.3 K), then, the validation is accepted [25]. However, if instrumental brightness temperatures are already biased, as is true for ECOSTRESS (Figure 5) and such biases are not the same for the two bands (−0.33 for BT12 and 0.23 for BT11; −0.58 and −0.09, respectively, when the ACF correction was applied), then, this radiance-based validation method may not correct the SST bias.

Most of the coefficient values estimated for each regression algorithm with the four different datasets (Table 1) were not within the published ranges obtained in other studies. This lack of match could be due to the different nature of the calibrations performed in those studies, as those were direct temperature comparisons between MODIS/VIIRS instruments and in situ measurements from ships, buoys, and drifters ([48], https://oceancolor.gsfc.nasa.gov/atbd/sst/#sec_2, accessed on 7 December 2021). Those comparisons are quite different from our ECOSTRESS-VIIRS-N20 multisensor intercomparison approach. After performing the spatial autocorrelation correction, coefficient estimates for some parameters were not significantly different from zero (Table 1). This was probably caused by the large reduction in the number of observations and degrees of freedom in the regression analyses following the spatial autocorrelation correction (Table 3). Note, however, that the R^2 values remained in excess of 0.99 in all cases (Table 2). Thus, despite this large reduction in the size of the available dataset, the goodness of fit of the calibration with VIIRS data and the estimation of the bias were not affected.

4.2. Biological and Oceanographic Implications of SST Bias

Many thermal properties have dramatic shifts over small temperature ranges; organism physiological performance curves and probabilities of mortality often are asymmetric with sharp clines near thermal limits. A 1 °C, cold bias could potentially impact the accuracy and sign of the predictions on the biological fitness of marine organisms based on ECOSTRESS data. For instance, mass mortality of mussels is known to have occurred along the northeastern Atlantic shores at temperatures of 32 °C [55,56]. Laboratory experiments showed a drop from 80% to 10% in survival rates between 30 and 32 °C, which emphasizes the importance of precise SST measurements in order to properly forecast high mortality events. Similarly, cumulative mortality curves as a function of time in different commercial clam species change dramatically between 32 and 36 °C [57]. Moreover, dispersal parameters for coastal invertebrate larvae and other propagules are severely affected by their metabolic rates which are, in turn, determined by temperature [58]. For example, planktonic larval duration (PLD) is known to exponentially decrease with SST, so a 1 °C cold bias can be translated to an artificial PLD overestimation of many days which may lead to erroneous calculations of dispersal distances [59,60].

The observed bias can also affect the utility of ECOSTRESS to infer climate change-driven upwelling dynamics between regions where Bakun´s upwelling intensification occurs and those where surface warming and stratification prevail. Thermal upwelling indexes, such as the ones used by [61,62] along the coasts of northern and southern Africa, respectively, will be altered by such a bias. These indexes are based on the horizontal offshore-onshore temperature contrast divided by the vertical temperature difference offshore. This denominator would be one degree lower if ECOSTRESS SST data were used, as it is calculated as offshore SST minus a constant bottom layer temperature characteristic of the water mass that upwells [62]. Thus, artificially high thermal upwelling indexes would result with the use of ECOSTRESS SST measurements. In fact, such potential upwelling overestimation reveals that indexes that incorporate constant parameters, such as the temperature of a deep-water mass, are more prone to errors produced by biases in satellite SST estimates.

4.3. Importance of Spatial Autocorrelation in Algorithm Selection

Our results show the importance of spatial autocorrelation in these calibration analyses. Because the e-folding distances were on the order of many tens of kms (8 to 125 km, Table S1), the dataset was reduced from 2,282,368 to 406 pixels when the autocorrelation correction was applied. These distances are consistent with the known patch size in SST derived from Moran´s I correlograms off the coast of Chile (a mean of 40 km approximately, [63]) and with the SST semivariance variograms performed for the Gulf of Mexico (75–300 km, [64]). Similarly, Moran's I z scores revealed SST spatial autocorrelation distances between 200 and 400 km off the northeastern coast of USA [65], while autocorrelation functions for SST fitted by normal distributions yielded scales from 80 to 300 km off Sicily [66]. The differences among all these estimates may be due to spatiotemporal variability in SST at different regions, to the slightly different methodologies that were applied, and especially, to differences in the size of the images that were analyzed (565 km for ECOSTRESS scenes of 400 × 400 km approximately). Regardless of the SST exact autocorrelation scale, spatial autocorrelation has to be considered in this kind of analysis. Failure to adjust for spatial autocorrelation reduces the independence of residuals, and thereby severely hinders hypothesis testing by erroneously inflating the statistical power to detect pattern. Following correction for spatial autocorrelation, our model selection procedure based on BIC changed. Although all the algorithms explained more than 99% of the SST variability, note that when the whole dataset was considered, NLSST, the most complex used algorithm, was selected as the best fit (Table 2) and the backward BIC model selection failed to remove any parameters from the initial model containing all the parameters (Model 1 in Table 3). However, with the reduced dataset after the spatial autocorrelation correction, a simpler algorithm, NAVO, was selected instead, and the backward BIC model selection led to the much simpler Model 2 (Tables 2 and 3). Although BIC penalizes model complexity more heavily when there is a large number of observations, the higher R^2 and lower RSE of the NLSST algorithm as compared with NAVO for the whole dataset clearly compensated for this effect. This compensation does not occur for the reduced dataset as differences in R^2 are close to zero; therefore, NAVO was chosen as the best fit (Table 2).

5. Conclusions

In summary, ECOSTRESS SST datasets have great potential for studies on temperature trends, upwelling dynamics, coastal oceanography, and distribution shifts of marine species given the global coverage and high spatial resolution of the instrument. Furthermore, its unprecedented small scale detail may reveal coastal oceanographic processes and structures unknown today [67]. It is true that the 1 °C cold bias in SST that we detected may introduce some level of uncertainty in comparative oceanographic and ecological studies between ECOSTRESS and other temperature datasets. Nevertheless, it is a uniform bias across a wide thermal range (from 0 to 35 °C), and therefore the thermal contrasts observed in oceanographic structures in ECOSTRESS imagery (Figure 3) are reliable. In addition, we show that the observed temperature bias can be corrected with the different regression algorithms presented in this study that are used on a regular basis to retrieve SST data for other satellite products. In this way, we avoid SST underestimations that are probably caused by the use of the TES algorithm. For satellite product users not involved in the calibration of these datasets, we propose a simpler solution in light of our results, i.e., to add a constant of 1 °C to ECOSTRESS SST. The goodness of fit and error estimates obtained from our raw VIIRS-ECOSTRESS calibrations are very similar to those derived from the regression algorithms we tested (see Section 2.1, Table 2 and Figure 8), illustrating that ECOSTRESS SST data plus 1 °C match remarkably well the reference VIIRS data. Thus, it is possible to easily correct this cold bias at both the user and data manager levels in order to take advantage of the unique characteristics of ECOSTRESS in future oceanographic and ecological studies.

Supplementary Materials: The following are available online at https://www.mdpi.com/article/10.3390/rs13245021/s1, Table S1: Details on ECOSTRESS-VIIRS-N20 comparisons.

Author Contributions: Conceptualization and methodology, N.W, D.S.W. and S.A.W.; data analysis, N.W. and D.S.W.; writing—original draft preparation, N.W.; writing—review and editing, S.A.W. and D.S.W.; data curation, D.S.W. and N.W. All authors have read and agreed to the published version of the manuscript.

Funding: This research was funded by NASA, grant number 80NSSC20K0074.

Institutional Review Board Statement: Not applicable.

Informed Consent Statement: Not applicable.

Data Availability Statement: The data that support the findings of this study are available from the corresponding author, upon request.

Acknowledgments: We would like to thank the GHRSST IC-TT Task 3 members and Jon Mittaz for their advice. This is contribution 107 in Ecological Forecasting from the University of South Carolina.

Conflicts of Interest: The authors declare no conflict of interest.

References

1. Levitus, S.; Antonov, J.I.; Boyer, T.P.; Baranova, O.K.; Garcia, H.E.; Locarnini, R.A.; Mishonov, A.V.; Reagan, J.R.; Seidov, D.; Yarosh, E.S.; et al. World Ocean Heat Content and Thermosteric Sea Level Change (0–2000 m), 1955–2010. *Geophys. Res. Lett.* **2012**, *39*, L10603. [CrossRef]
2. Alexander, L.V.; Allen, S.K.; Bindoff, N.L.; Bréon, F.-M.; Church, J.A.; Cubasch, U.; Emori, S.; Forster, P.; Friedlingstein, P.; Gillett, N.; et al. *Climate Change 2013: The Physical Science Basis: Summary for Policymakers, a Report of Working Group I to the Fifth Assessment Report of the IPCC*; Stocker, T., Qin, D., Plattner, G.K., Tignor, M., Allen, S.K., Boschung, J., Nauels, A., Xia, Y., Bex, V., Midgley, P.M., Eds.; Cambridge University Press: Cambridge, UK; New York, NY, USA, 2013; p. 1535. Available online: https://www.ipcc.ch/site/assets/uploads/2018/02/WG1AR5_SPM_FINAL.pdf (accessed on 7 December 2021).
3. Baringer, M.; Bif, M.B.; Boyer, T.; Bushinsky, S.M.; Carter, B.R.; Cetinić, I.; Chambers, D.P.; Cheng, L.; Chiba, S.; Dai, M.; et al. Global Oceans. *Bull. Am. Meteorol. Soc.* **2020**, *101*, S129–S184. [CrossRef]
4. Johnson, G.C.; Lyman, J.M. Warming Trends Increasingly Dominate Global Ocean. *Nat. Clim. Chang.* **2020**, *10*, 757–761. [CrossRef]
5. Gruber, N.; Clement, D.; Carter, B.R.; Feely, R.A.; van Heuven, S.; Hoppema, M.; Ishii, M.; Key, R.M.; Kozyr, A.; Lauvset, S.K.; et al. The Oceanic Sink for Anthropogenic CO_2 from 1994 to 2007. *Science* **2019**, *363*, 1193–1199. [CrossRef] [PubMed]
6. Dangendorf, S.; Marcos, M.; Wöppelmann, G.; Conrad, C.P.; Frederikse, T.; Riva, R. Reassessment of 20th Century Global Mean Sea Level Rise. *Proc. Natl. Acad. Sci. USA* **2017**, *114*, 5946–5951. [CrossRef] [PubMed]
7. Kulp, S.A.; Strauss, B.H. New Elevation Data Triple Estimates of Global Vulnerability to Sea-Level Rise and Coastal Flooding. *Nat. Commun.* **2019**, *10*, 4844. [CrossRef] [PubMed]
8. Reguero, B.G.; Losada, I.J.; Méndez, F.J. A Recent Increase in Global Wave Power as a Consequence of Oceanic Warming. *Nat. Commun.* **2019**, *10*, 205. [CrossRef] [PubMed]
9. Legeckis, R.; Gordon, A.L. Satellite Observation of the Brazil and Fakland Currents-1975 to 1976 and 1978. *Deep Sea Res.* **1982**, *3A*, 375–401. [CrossRef]
10. Minnett, P.J.; Kilpatrick, K.A.; Podestá, G.P.; Evans, R.H.; Szczodrak, M.D.; Izaguirre, M.A.; Williams, E.J.; Walsh, S.; Reynolds, R.M.; Bailey, S.W.; et al. Skin Sea-Surface Temperature from VIIRS on Suomi-NPP—NASA Continuity Retrievals. *Remote Sens.* **2020**, *12*, 3369. [CrossRef]
11. Emery, W.J.; Castro, S.; Wick, G.A.; Schluessel, P. Estimating sea surface temperature from infrared satellite and in situ temperature data. *Bull. Am. Meteorol. Soc.* **2001**, *82*, 2773–2786. [CrossRef]
12. Schloesser, F.; Cornillon, P.; Donohue, K. Evaluation of Termosalinograph and VIIRS Data for the Characterization of Near Surface Temperature Fields. *J. Atmos. Ocean. Tecnol.* **2016**, *33*, 1843–1858. [CrossRef]
13. Li, X.; Pichel, W.; Clemente-Colón, P.; Krasnopolsky, V.; Sapper, J. Validation of Coastal Sea and Lake Surface Temperature Measurements Derived from NOAA/AVHRR Data. *Int. J. Remote Sens.* **2001**, *22*, 1285–1303. [CrossRef]
14. Zhang, H.-M. Bias Characteristics in the AVHRR Sea Surface Temperature. *Geophys. Res. Lett.* **2004**, *31*, L01307. [CrossRef]
15. Lima, F.P.; Wethey, D.S. Three Decades of High-Resolution Coastal Sea Surface Temperatures Reveal More than Warming. *Nat. Commun.* **2012**, *3*, 704. [CrossRef] [PubMed]
16. Bakun, A.; Black, B.A.; Bograd, S.J.; García-Reyes, M.; Miller, A.J.; Rykaczewski, R.R.; Sydeman, W.J. Anticipated Effects of Climate Change on Coastal Upwelling Ecosystems. *Curr. Clim. Chang. Rep.* **2015**, *1*, 85–93. [CrossRef]
17. Seabra, R.; Varela, R.; Santos, A.M.; Gómez-Gesteira, M.; Meneghesso, C.; Wethey, D.S.; Lima, F.P. Reduced nearshore warming associated with eastern boundary upwelling systems. *Front. Mar. Sci.* **2019**, *6*, 104. [CrossRef]

18. Canales, T.M.; Lima, M.; Wiff, R.; Contreras-Reyes, J.E.; Cifuentes, U.; Montero, J. Endogenous, Climate, and Fishing Influences on the Population Dynamics of Small Pelagic Fish in the Southern Humboldt Current Ecosystem. *Front. Mar. Sci.* **2020**, *7*, 82. [CrossRef]
19. Bakun, A. Global Climate Change and Intensification of Coastal Upwelling. *Science* **1990**, *247*, 198–201. [CrossRef]
20. Cordeiro Pires, A.; Nolasco, R.; Rocha, A.; Ramos, A.M.; Dubert, J. Climate Change in the Iberian Upwelling System: A Numerical Study Using GCM Downscaling. *Clim. Dyn.* **2016**, *47*, 451–464. [CrossRef]
21. Sousa, M.C.; Ribeiro, A.; Des, M.; Gomez-Gesteira, M.; deCastro, M.; Dias, J.M. NW Iberian Peninsula Coastal Upwelling Future Weakening: Competition between Wind Intensification and Surface Heating. *Sci. Total Environ.* **2020**, *703*, 134808. [CrossRef]
22. García-Reyes, M.; Largier, J. Observations of Increased Wind-Driven Coastal Upwelling off Central California. *J. Geophys. Res.* **2010**, *115*, C04011. [CrossRef]
23. Weidberg, N.; Ospina-Alvarez, A.; Bonicelli, J.; Barahona, M.; Aiken, C.M.; Broitman, B.R.; Navarrete, S.A. Spatial Shifts in Productivity of the Coastal Ocean over the Past Two Decades Induced by Migration of the Pacific Anticyclone and Bakun's Effect in the Humboldt Upwelling Ecosystem. *Glob. Planet. Chang.* **2020**, *193*, 103259. [CrossRef]
24. Hulley, G.C.; Hook, S.J. Level 2 Land Surface Temperature and Emissivity Algorithm Theoretical Basis Document (ATBD). *NASA JPL Rep.* **2015**. Available online: https://ecostress.jpl.nasa.gov/downloads/atbd/ECOSTRESS_L2_ATBD_LSTE_2018-03-08.pdf (accessed on 7 December 2021).
25. Hulley, G.C.; Göttsche, F.M.; Rivera, G.; Hook, S.J.; Freepartner, R.J.; Martin, M.A.; Cawse-Nicholson, K.; Johnson, W.R. Validation and Quality Assessment of the ECOSTRESS Level-2 Land Surface Temperature and Emissivity Product. *IEEE Trans. Geosci. Remote Sens.* **2021**, 1–23. [CrossRef]
26. Hook, S.J.; Cawse-Nicholson, K.; Barsi, J.; Radocinski, R.; Hulley, G.C.; Johnson, W.R.; Rivera, G.; Markham, B. In-Flight Validation of the ECOSTRESS, Landsats 7 and 8 Thermal Infrared Spectral Channels Using the Lake Tahoe CA/NV and Salton Sea CA Automated Validation Sites. *IEEE Trans. Geosci. Remote Sens.* **2020**, *58*, 1294–1302. [CrossRef]
27. Shi, J.; Hu, C. Evaluation of ECOSTRESS Thermal Data over South Florida Estuaries. *Sensors* **2021**, *21*, 4341. [CrossRef]
28. Xiong, X.; Angal, A.; Chang, T.; Chiang, K.; Lei, N.; Li, Y.; Sun, J.; Twedt, K.; Wu, A. MODIS and VIIRS Calibration and Characterization in Support of Producing Long-Term High-Quality Data Products. *Remote Sens.* **2020**, *12*, 3167. [CrossRef]
29. Wang, W.; Cao, C. Monitoring the NOAA Operational VIIRS RSB and DNB Calibration Stability Using Monthly and Semi-Monthly Deep Convective Clouds Time Series. *Remote Sens.* **2016**, *8*, 32. [CrossRef]
30. Cao, C.; Xiong, J.; Blonski, S.; Liu, Q.; Uprety, S.; Shao, X.; Bai, Y.; Weng, F. Suomi NPP VIIRS Sensor Data Record Verification, Validation, and Long-Term Performance Monitoring. *J. Geophys. Res. Atmos.* **2013**, *118*, 11664–11678. [CrossRef]
31. Cao, C.; Wang, W.; Blonski, S.; Zhang, B. Radiometric traceability diagnosis and bias correction for the suomi npp viirs long-wave infrared channels during blackbody unsteady states. *J. Geophys. Res. Atmos.* **2017**, *122*, 5285–5297. [CrossRef]
32. Govekar, P.; Mittaz, J.; Griffin, C.; Beggs, H. Himawari-8 and Multi Sensor Sea Surface Temperature Products and Their Application. In Proceedings of the GXXII Virtual Meeting, Virtual, 7–11 June 2021.
33. Good, S.; Fiedler, E.; Mao, C.; Martin, M.J.; Maycock, A.; Reid, R.; Roberts-Jones, J.; Searle, T.; Waters, J.; While, J.; et al. The Current Configuration of the OSTIA System for Operational Production of Foundation Sea Surface Temperature and Ice Concentration Analyses. *Remote Sens.* **2020**, *12*, 720. [CrossRef]
34. Hook, S.; Smyth, M.; Logan, T.; Johnson, W. ECOSTRESS Cloud Mask Daily L2 Global 70m V001 [Data set]. NASA EOSDIS Land Processes DAAC. 2019. Available online: https://doi.org/10.5067/ECOSTRESS/ECO2CLD.001 (accessed on 7 December 2021).
35. Hook, S.; Hulley, G. ECOSTRESS Land Surface Temperature and Emissivity Daily L2 Global 70 m V001 [Data set]. NASA EOSDIS Land Processes DAAC. 2019. Available online: https://doi.org/10.5067/ECOSTRESS/ECO2LSTE.001 (accessed on 7 December 2021).
36. Hook, S.; Smyth, M.; Logan, T.; Johnson, W. ECOSTRESS at-Sensor Calibrated Radiance Daily L1B Global 70 m V001 [Data set]. NASA EOSDIS Land Processes DAAC. 2019. Available online: https://doi.org/10.5067/ECOSTRESS/ECO1BRAD.001 (accessed on 7 December 2021).
37. Hook, S.; Smyth, M.; Logan, T.; Johnson, W. ECOSTRESS Geolocation Daily L1B Global 70 m V001 [Data set]. NASA EOSDIS Land Processes DAAC. 2019. Available online: https://doi.org/10.5067/ECOSTRESS/ECO1BGEO.001 (accessed on 7 December 2021).
38. NOAA. NOAA Office of Satellite and Product Operations (OSPO). Sea Surface Temperature Retrievals Produced by NOAA/NESDIS/OSPO Office from VIIRS Sensor. Ver. 2.61. PO.DAAC, CA, USA. 2019. Available online: https://doi.org/10.5067/GHV20-2PO61 (accessed on 24 September 2021).
39. Petrenko, B.; Ignatov, A.; Kihai, Y.; Stroup, J.; Dash, P. Evaluation and Selection of SST Regression Algorithms for JPSS VIIRS. *J. Geophys. Res. Atmos.* **2014**, *119*, 4580–4599. [CrossRef]
40. Canada Meteorological Center. CMC 0.1 Deg Global Sea Surface Temperature Analysis. Ver. 3.0. PO.DAAC, CA, USA. 2016. Available online: https://doi.org/10.5067/GHCMC-4FM03 (accessed on 24 September 2021).
41. Saha, K.; Ignatov, A.; Liang, X.M.; Dash, P. Selecting a first-guess sea surface temperature field as input to forward radiative transfer models. *J. Geophys. Res. Ocean.* **2012**, *117*, C12001. [CrossRef]
42. Krehbiel, C. ECOSTRESS Swath to Grid Conversion Script. 2021. Available online: https://git.earthdata.nasa.gov/projects/LPDUR/repos/ecostress_swath2grid/browse (accessed on 24 September 2021).
43. Baddeley, A. Package Spatsat 1.31-1 in R. Available online: https://cran.r-project.org/package=spatstat (accessed on 7 December 2021).

44. Legendre, P. Spatial Autocorrelation: Trouble or Paradigm? *Ecology* **1993**, *74*, 1659–1673. [CrossRef]
45. Venables, W.N.; Ripley, B.D. *Modern Applied Statistics with S*, 4th ed.; Springer: Cham, Switzerland, 2002.
46. Ding, R.; Li, J. Influences of ENSO Teleconnection on the Persistence of Sea Surface Temperature in the Tropical Indian Ocean. *J. Clim.* **2012**, *25*, 8177–8195. [CrossRef]
47. Bulgin, C.E.; Merchant, C.J.; Ferreira, D. Tendencies, Variability and Persistence of Sea Surface Temperature Anomalies. *Sci. Rep.* **2020**, *10*, 7986. [CrossRef] [PubMed]
48. McBride, W.; Arnone, R.; Cayula, J.-F. Improvements of Satellite SST Retrievals at Full Swath. *Proc. SPIE* **2013**, *8724*, 87240R. [CrossRef]
49. Donlon, C.J.; minnett, P.J.; Gentemann, C.; Nightingale, T.J.; Barton, I.J.; Ward, B.; Murray, M.J. Toward Improved Validation of Satellite Sea Surface Skin Temperature Measurements for Climate Research. *J. Clim.* **2002**, *15*, 353–369. [CrossRef]
50. Merchant, C.J.; Harris, A.R.; Murray, M.J.; Závody, A.M. Toward the Elimination of Bias in Satellite Retrievals of Sea Surface Temperature: 1. Theory, Modeling and Interalgorithm Comparison. *J. Geophys. Res. Ocean.* **1999**, *104*, 23565–23578. [CrossRef]
51. Merchant, C.J.; Harris, A.R. Toward the Elimination of Bias in Satellite Retrievals of Sea Surface Temperature: 2. Comparison with in Situ Measurements. *J. Geophys. Res. Ocean.* **1999**, *104*, 23579–23590. [CrossRef]
52. Gillespie, A.R.; Matsunaga, T.; Rokugawa, S.; Hook, J. Temperature and Emissivity Separation from Advanced Spaceborne Thermal Emission and Reflection Radiometer (ASTER) Images. *IEEE Trans. Geosci. Remote Sens.* **1998**, *36*, 1113–1125. [CrossRef]
53. Saunders, R.W.; Blackmore, T.A.; Candy, B.; Francis, P.N.; Hewison, T.J. Monitoring Satellite Radiance Biases Using NWP Models. *IEEE Trans. Geosci. Remote Sens.* **2013**, *51*, 1124–1138. [CrossRef]
54. Matricardi, M. Technical Note: An Assessment of the Accuracy of the RTTOV Fast Radiative Transfer Model Using IASI Data. *Atmos. Chem. Phys.* **2009**, *9*, 6899–6913. [CrossRef]
55. Jones, S.J.; Mieszkowska, N.; Wethey, D.S. Linking thermal tolerances and biogeography: *Mytilus edulis* (L.) at its southern limit on the east coast of the United States. *Biol. Bull.* **2009**, *217*, 73–85. [CrossRef]
56. Jones, S.J.; Lima, F.P.; Wethey, D.S. Rising Environmental Temperatures and Biogeography: Poleward Range Contraction of the Blue Mussel, *Mytilus Edulis* L., in the Western Atlantic: Mytilus Edulis Poleward Range Contraction. *J. Biogeogr.* **2010**, *37*, 2243–2259. [CrossRef]
57. Macho, G.; Woodin, S.A.; Wethey, D.S.; Vázquez, E. Impacts of Sublethal and Lethal High Temperatures on Clams Exploited in European Fisheries. *J. Shellfish. Res.* **2016**, *35*, 405–419. [CrossRef]
58. Crickenberger, S.; Wethey, D.S. Annual Temperature Variation as a Time Machine to Understand the Effects of Long-Term Climate Change on a Poleward Range Shift. *Glob. Chang. Biol.* **2019**, *23*, 3804–3819. [CrossRef] [PubMed]
59. O'Connor, M.I.; Bruno, J.F.; Gaines, S.D.; Halpern, B.S.; Lester, S.E.; Kinlan, B.P.; Weiss, J.M. Temperature Control of Larval Dispersal and the Implications for Marine Ecology, Evolution, and Conservation. *Proc. Natl. Acad. Sci. USA* **2007**, *104*, 1266–1271. [CrossRef] [PubMed]
60. White, J.; Botsford, L.; Hastings, A.; Largier, J. Population Persistence in Marine Reserve Networks: Incorporating Spatial Heterogeneities in Larval Dispersal. *Mar. Ecol. Prog. Ser.* **2010**, *398*, 49–67. [CrossRef]
61. Demarcq, H.; Faure, V. Coastal Upwelling and Associated Retention Indices Derived from Satellite SST. Application to Octopus vulgaris Recruitment. *Oceanol. Acta* **2000**, *23*, 391–408. [CrossRef]
62. Pfaff, M.; Branch, G.; Wieters, E.; Branch, R.; Broitman, B. Upwelling Intensity and Wave Exposure Determine Recruitment of Intertidal Mussels and Barnacles in the Southern Benguela Upwelling Region. *Mar. Ecol. Prog. Ser.* **2011**, *425*, 141–152. [CrossRef]
63. Lagos, N.; Navarrete, S.; Véliz, F.; Masuero, A.; Castilla, J. Meso-Scale Spatial Variation in Settlement and Recruitment of Intertidal Barnacles along the Coast of Central Chile. *Mar. Ecol. Prog. Ser.* **2005**, *290*, 165–178. [CrossRef]
64. Kleisner, K.; Walter, J.; Diamond, S.; Die, D. Modeling the Spatial Autocorrelation of Pelagic Fish Abundance. *Mar. Ecol. Prog. Ser.* **2010**, *411*, 203–213. [CrossRef]
65. Jossart, J.; Theuerkauf, S.J.; Wickliffe, L.C.; Morris, J.A., Jr. Applications of Spatial Autocorrelation Analyses for Marine Aquaculture Siting. *Front. Mar. Sci.* **2020**, *6*, 806. [CrossRef]
66. Borzelli, G.; Ligi, R. Autocorrelation Scales of the SST Distribution and Water Masses Stratification in the Channel of Sicily. *J. Atmos. Ocean Tech.* **1999**, *16*, 776–781. [CrossRef]
67. Weidberg, N.; Woodin, S.A.; Wethey, D.S. Ultra-High Resolution SST from NASA ECOSTRESS Resolves Fine Structure of Upwelling Zones. In Proceedings of the GXXII Virtual Meeting, Virtual, 7–11 June 2021.